scientific reports

OPEN

Design and fabrication of a semi-transparent solar cell considering the effect of the layer thickness of MoO₃/Ag/MoO₃ transparent top contact on optical and electrical properties

Çağlar Çetinkaya[1,2✉], Erman Çokduygulular[3], Barış Kınacı[1], Feyza Güzelçimen[1], Yunus Özen[4,5], Halil İbrahim Efkere[5,6], İdris Candan[7], Serkan Emik[8] & Süleyman Özçelik[5,9]

We conducted the present study to design and manufacture a semi-transparent organic solar cell (ST-OSC). First, we formed a transparent top contact as MoO₃/Ag/MoO₃ in a dielectric/metal/dielectric (DMD) structure. We performed the production of an FTO/ZnO/P3HT:PCBM/MoO₃/Ag/MoO₃ ST-OSC by integrating MoO₃/Ag/MoO₃ (10/d_m/d_{od} nm) instead of an Ag electrode in an opaque FTO/ZnO/ P3HT:PCBM/MoO₃/Ag (–/40/130/10/100 nm) OSC, after theoretically achieving optimal values of optical and electrical parameters depending on Ag layer thickness. The transparency decreased with the increase of d_m values for current DMD. Meanwhile, maximum transmittance and average visible transmittance (AVT) indicated the maximum values of over 92% for d_m = 4 and 8 nm, respectively. For ST-OSCs, the absorption and reflectance increased in the visible region by a wavelength of longer than 560 nm and in the whole near-infrared region by increasing d_m up to 16 nm. Moreover, in the CIE chromaticity diagram, we reported a shift towards the D65 Planckian locus for colour coordinates of current ST-OSCs. Electrical analysis indicated the photogenerated current density and AVT values for d_m = 6 nm as 63.30 mA/cm² and 38.52%, respectively. Thus, the theoretical and experimental comparison of optical and electrical characteristics confirmed that the manufactured structure is potentially conducive for a high-performance ST-OSC.

Organic solar cells (OSC), where organic materials form the active region, are very useful in terms of low-cost production and fabrication processes, flexibility, lightness and roll-to-roll printability[1–5]. Though in the past, the power conversion efficiency (PCE) values of inorganic semiconductor-based solar cells were much higher than OSCs, today, the PCE of OSCs has raised over 18%[6,7]. In addition, many studies have been conducted to improve PCE, such as the adoption of solvent additives, the use of various active layers, the use of thermal or solvent annealing processes and the use of the triple strategy and reverse structure cells[7–13].

The optical band gap of organic semiconductor materials can be easily tuned. The thickness of organic active layers in OSC-based photovoltaic technology is about one hundred nanometres for adequate photon harvesting. The ability to form structures, which are thin and have high absorbance, has created the potential to design a semi-transparent organic solar cell (ST-OSC), which has photon harvesting in the near-infrared range and

[1]Physics Department, Faculty of Science, Istanbul University, 34134 Istanbul, Turkey. [2]Graduate School of Engineering and Science, Istanbul University, 34116 Istanbul, Turkey. [3]Department of Engineering Sciences, Faculty of Engineering, Istanbul University-Cerrahpaşa, 34320 Istanbul, Turkey. [4]Department of Physics, Faculty of Science, Gazi University, 06500 Ankara, Turkey. [5]Photonics Application and Research Center, Gazi University, 06500 Ankara, Turkey. [6]Deparment of Metallurgical and Materials Engineering, Faculty of Technology, Gazi University, 06500 Ankara, Turkey. [7]Department of Physics, Kocaeli University, 41001 İzmit, Kocaeli, Turkey. [8]Department of Chemical Engineering, Faculty of Engineering, Istanbul University-Cerrahpaşa, 34320 Istanbul, Turkey. [9]Department of Photonics, Faculty of Applied Sciences, Gazi University, 06500 Ankara, Turkey. ✉email: caglarcetinkaya@istanbul.edu.tr

1

transmittance in the visible light region. When the necessary adjustment and modification is made in the ST-OSC structure, the transparency can be effectively achieved in the visible region (VR) of the solar spectrum as well as it can also absorb light in the NIR region[7]. Thus, the use of ST-OSCs enables the design of state-of-the-art window and curtain applications that can convert sunlight in order to generate electrical power.

For greenhouse applications, because chlorophylls function in a small range of the light spectrum, ST-OSCs can be adjusted to be highly transparent over the spectrum that is required for plant growth[14–16]. Especially in the building industry, building-integrated photovoltaic (BIPV) technology is becoming one of the most effective techniques to power buildings with renewable energy[14,17]. ST-OSCs' translucence not only provides them to operate as a generator but also reduces electricity consumption by allowing natural light to pass through[17]. The application of ST-OSCs on windows in buildings can enable social living areas with smart and healthy home technologies to receive sunlight.

The top contact material used in inverted OSC is made with thick metal electrodes, such as Ag, Au, and Al, which are highly reflective in VR[18]. Regardless of the optical transmittance and reflection properties of the polymer structure forming the active region, the transmittance characteristic of the OSC is determined by the top contact. Hence, the structure becomes completely opaque. One of the most vital steps of ST-OSC design is to make a top contact with high conductivity and optical transmittance, especially in the VR. In the meanwhile, double-sided transparent solar cells enable light response in optoelectronic device applications[19,20]. Besides improving the PCE value of the ST-OSC structure for practical applications, the average visible transmittance (AVT) is expected to be at least 25%[18,21,22]. Though the transparency of ST-OSC is improved in the optimization of the AVT values of the top contact material, its absorption may decrease below AM 1.5G. This occurs low photo-generated current density (J_{ph}) and a decrease in PCE values. With the increase of the thickness of active region, the J_{ph} and PCE values of the ST-OSC have improved, while the optical characteristics and AVT values may seriously deteriorate. Therefore, there is a trade-off, which makes the optics inside the device more critical between photovoltaic performance and the visible transparency of the device. Appropriate selection of material and adjustion of its thickness are simultaneously optimized to achieve good conductivity and high AVT for the top electrode[7].

For the purpose of semi-transparency in ST-OSC design, a thin metal material is sandwiched between two anti-reflection dielectrics as the top contact and a dielectric/metal/dielectric (DMD) structure is formed[23]. DMD designs offer high transparency and conductivity, low turbidity, excellent flexibility, easy fabrication and excellent compatibility with different substrates[24–36]. Therefore, it is clear that ST DMDs have a strong future, especially in ST optoelectronic devices[15,20,37–40]. An ST DMD electrode is designed to be able to fabricate ultra-thin metallic films and to improve the conductivity and flexibility of indium tin oxide (ITO). Recently, it has been used to replace ITO in SC applications[41]. DMD electrodes have taken a vital place in the design of OSC structures as ST. Even if the OSCs are grown over ITO, it is possible to make the opaque top contact transparent and the SC to become ST with the appropriate design of DMD structures[40]. It is noteworthy that DMD structures have simple fabrication processes and simple designs that do not require microscale or nanoscale shaping, such as photonic crystals[42,43]. Due to the inherently low reflectivity of the transparent electrodes, the photon absorption of the device must be carefully adjusted to allow sufficient light to pass through the device[18].

In the present study, a $MoO_3/Ag/MoO_3$ transparent top contact in DMD structure was designed for opaque P3HT:PCBM-based OSCs in inverted structure architecture. We also studied the integration of DMD into OSC structure at optimal thickness values. In this context, we determined the optimal thickness values of both $MoO_3/Ag/MoO_3$ integrated into the FTO/ZnO/P3HT:PCBM/MoO_3/Ag opaque-OSC structure and the current designed FTO/ZnO/P3HT:PCBM/MoO_3/Ag/MoO_3 ST-OSC structure based on the theoretical AVT and J_{ph} values in the optical spectra calculated via transfer matrix method (TMM). We just focused on examination the CIE 1931 chromaticity coordinates of the structures depending on metal layer thickness. We optically characterized as well as the cell output parameters of ST-OSC designed and produced with optimal values were computed. Besides, a comparative evaluation of the calculated and experimantally obtained values was conducted.

Results

The FTO/ZnO/P3HT:PCBM/MoO_3/Ag opaque-OSC structure has Ag top electrode with a thickness of 100 nm. Ag has a very high reflectivity and low transmittance, especially in the VR. Thus, using Ag for top contact makes the OSC have opaque characteristics. We designed the ST-OSC by modifying the opaque Ag top contact of the structure using a $MoO_3/Ag/MoO_3$ DMD transparent top electrode with appropriate design parameters. In the DMD, the thickness of the inner dielectric MoO_3 (d_{id}), the thickness of the metal layer (d_m) and the thickness of the outer dielectric MoO_3 (d_{od}) are parameters that considerably affect the optical characteristics of the OSC. Among these parameters, d_m is a significant value defining the optical properties of the DMD and ST-OSC due to the optical characteristics of Ag. In addition, the inner MoO_3 layer is directly integrated above the active layer P3HT:PCBM, so the layer also acts as the hole transport layer (HTL). The d_{id} value can also influence output cell parameters, such as open-circuit voltage (V_{oc}), short-circuit current density (J_{sc}), maximum voltage (V_m), maximum current density (J_m), maximum power (P_m), PCE and fill factor (FF). Although the high thickness of the d_{id} may adversely affect the electrical properties of the ST-OSC, it is known that it does not dramatically cause an impact on the optical properties, especially on AVT[44]. Since the photo-generated free carriers formed in the active area are swept to the contacts by the internal electric field, if the distance between the contacts and the active region is greater than the diffusion lengths, the free carriers may disappear by recombination. Therefore, the carriers cannot contribute to the current and cell output parameters may be adversely affected. Because the electrical contact is taken directly from the metal layer on which outer dielectric is located, the effects of d_m and d_{od} values on the ST-OSC output cell parameters are only possible by modifying the optical spectra of the structure.
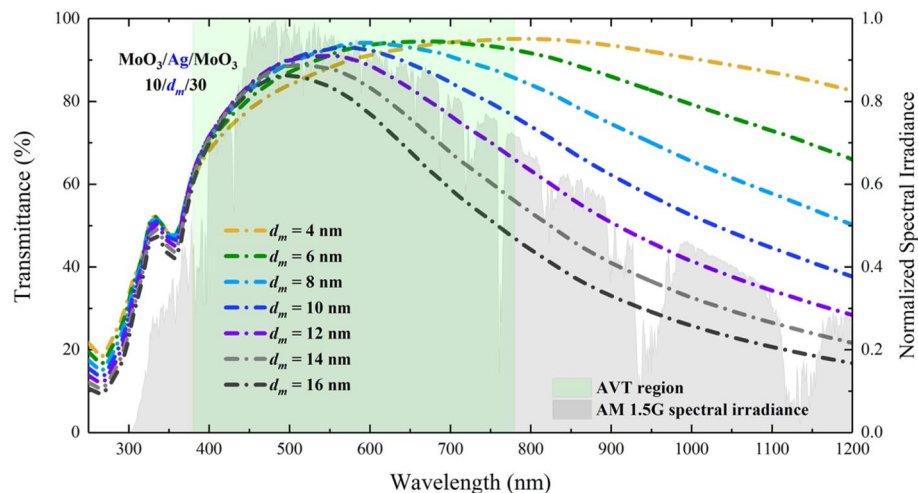
Figure 1. Calculated transmittance spectra of $MoO_3/Ag/MoO_3$ (10 nm/d_m/30 nm) DMD transparent top contact. The green shaded area shows the region where AVT is calculated.
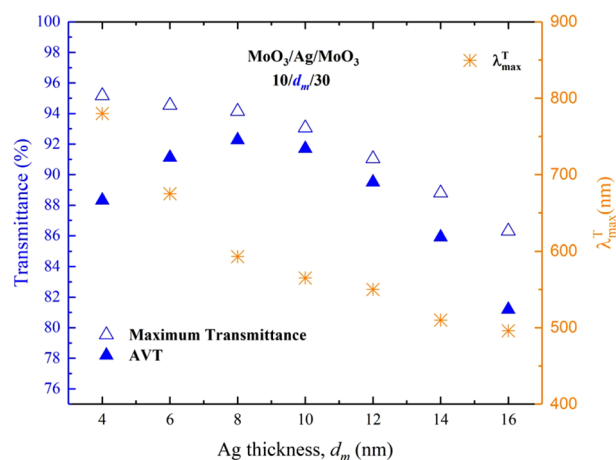

Figure 2. Changes of maximum transmittance, λ_{max}^{T} and AVT values of $MoO_3/Ag/MoO_3$ (10 nm/d_m/30 nm) DMD transparent top contact according to d_m.

For the reasons mentioned above, we first examined the effect of the d_m value on optical properties in the design of DMD and ST-OSC. We made the design of DMDs integrated to the OSC by calculating optical spectra, such as transmittance and reflection spectra, and especially by evaluating the thickness parameters.

First, $d_{id} = 10$ nm and $d_{od} = 30$ nm have been set for the inner and outer MoO_3 layers in TMM calculations, respectively. It is noticed that the d_{id} value usually ranges between 1 and 10 nm[45–48]. For the d_{od}, we have chosen 30 nm because Chang et al. reported that the highest AVT value was observed for this value in $MoO_3/Ag/MoO_3$ structure[14]. Therefore, we took the chosen value of d_{od} as a reference at the beginning of the calculations.

The d_m was changed between 4 and 16 nm with intervals of 2 nm, and we determined the effect of the Ag layer in DMD on the transmittance spectrum (Fig. 1). As seen in Fig. 1, for $MoO_3/Ag/MoO_3$ (10/d_m/30 nm), the transmittance is high for almost all investigated d_m values, and we observed that the transmittance spectrum has the same trend with AM 1.5G spectral irradiance. This indicates that the DMD is a favourable transparent top electrode. Due to the high reflectivity of Ag at all wavelengths where AM 1.5G is responsible, increasing the d_m value makes a decrease in the overall transmittance trend and especially in the maximum transmittance of the structure. When the DMD is integrated into ST-OSCs, the long wavelength of VR and the entire NIR will enhance the possibility of the re-absorption of unabsorbed electromagnetic waves as a result of the reflection of the electromagnetic waves to the active area. Thus, an improvement will occur in J_{ph} and PCE values. Another remarkable result is that the wavelength value (λ_{max}^{T}) at which the DMD transmittance spectrum has maximum transmittance decreased from 780 to 496 nm by varying d_m from 4 to 16 nm (Fig. 2).

The transmittance characteristic of the ST-OSC with DMD is quite limited by the optical characteristics of the DMD. The AVT values of the ST-OSC will be related to the AVT values of the DMD. AVT values obtained from the calculated transmittance spectra of DMD are given in Fig. 2. For the thinnest Ag layer ($d_m = 4$ nm), DMD has a maximum transmittance of 95.17%. This value is a result of the known reflectance and transmittance
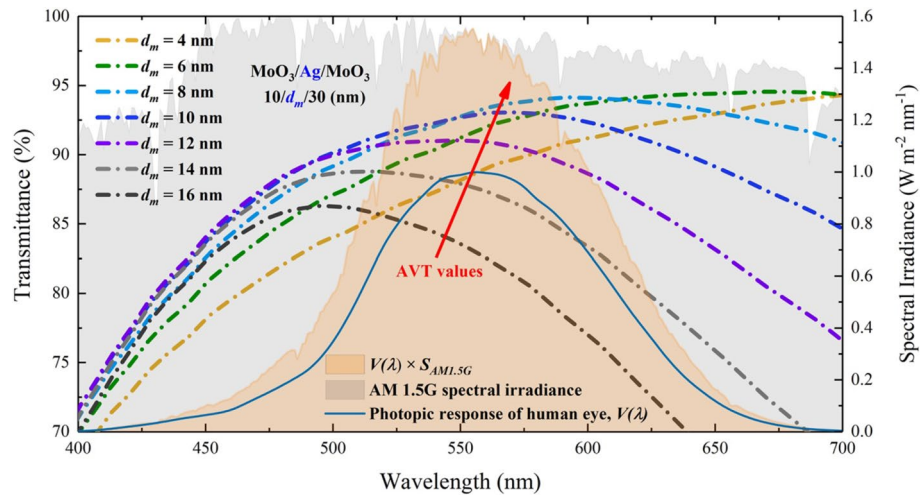
Figure 3. Analysis of the transmittance spectrum and AVT values of the MoO$_3$/Ag/MoO$_3$ (10 nm/d_m/30 nm) transparent top contact under $V(\lambda)$, AM 1.5G and $V(\lambda) \times S_{AM1.5G}(\lambda)$ changes. The orange shaded area is related to the change of $V(\lambda) \times S_{AM1.5G}(\lambda)$ and the area is the value of the integral in the denominator of Eq. (15).

characteristics of Ag. However, there is an increment in AVT values from 88.32 to 92.26% with the change of d_m from 4 to 8 nm. For $d_m > 8$ nm, the AVT value tends to decrease to 81.19% (for $d_m = 16$ nm). A maximum AVT value of 92.26% in DMD was found for $d_m = 8$ nm. According to these results, Ag is an optimal structure to be used in ST-OSCs for DMD when $d_m = 8$ nm.

T_{max} value is not achieved for the structure that has the highest AVT. It is due to the fact that the AVT criterion is directly connected to $V(\lambda)$ and $S_{AM1.5G}(\lambda)$, as mentioned in Eq. (16). It should not always be expected that the AVT value of an optimal structure with high optical transmittance is high. It should be taken into consideration that the selectivity and response of the human eye for different wavelengths are also important in perception for window applications. As seen in Fig. 3, the mismatch between transmittance and AVT relationship in DMD can be noticed.

The wavelength range of the human eye is sensitive in the range of 400–700 nm, and Eq. (16) includes $V(\lambda) \times S_{AM1.5G}(\lambda)$ multiply both the numerator and denominator. Therefore, even though the integral boundaries are over VR of the electromagnetic spectrum, integrants have values in the 400–700 nm range (Fig. 3). As seen in Fig. 3, it belongs to the structure of $d_m = 8$ nm with the highest transmittance value within the orange hatched area representing the $V(\lambda) \times S_{AM1.5G}(\lambda)$ expression, and the AVT of this structure is also the highest. The maximum transmittance is observed for $d_m = 4$ nm in the DMD, whereas the highest AVT value is obtained for $d_m = 8$ nm. The red arrow orientation in Fig. 3 indicates the variation of AVT. In the light of all these explanations, the transmittance characteristic of a structure does not directly give information about its AVT; an analysis as in Fig. 3 provides a more accurate AVT assessment.

The DMD produced with $d_m = 8$ nm, which belongs to the highest AVT, is very suitable for ST optoelectronic devices. However, the optical characteristics of the optoelectronic device to be produced with this DMD cannot be designed based only on the detailed examination for MoO$_3$/Ag/MoO$_3$. This is because in the TMM calculations made for MoO$_3$/Ag/MoO$_3$, the modelling is made with electromagnetic waves coming perpendicularly to the surface. However, the presence of the DMD in ST optoelectronic devices should be re-evaluated because the electromagnetic wave can follow different paths as a result of reflection, refraction or absorption in different regions until it reaches the DMD by passing through the OSC. The angle and condition in which the components of the electromagnetic wave reach the inner dielectric surface should also be taken into account. Thus, TMM calculations should be made for the entire structure of the optoelectronic device, and the optimal structure parameters should be determined.

We performed the optical characterization of the ST-OSC structure formed by the integration of the MoO$_3$/Ag/MoO$_3$ (10/d_m/d_{od} nm) instead of the Ag. We calculated the optical characteristics of FTO/ZnO/P3HT:PCBM/MoO$_3$/Ag/MoO$_3$ (–/40/130/10/d_m/30 nm) ST-OSC according to the d_m change by setting $d_{id} = 10$ nm and $d_{od} = 30$ nm. The calculated absorbance, reflectance and transmittance spectrum are shown in Fig. 4a–c, respectively. The characteristic of the absorbance spectrum of the ST-OSC structure is the same of which the P3HT:PCBM for all wavelengths (in Fig. 4a as an inset).

With the change of the d_m value, an enhancement occurs in the absorbance and reflectance of the ST-OSC in VR (longer than 560 nm) and NIR. While this rate of change is especially effective in the 4–10 nm range of d_m for absorption, it loses its effectiveness after $d_m = 10$ nm (Fig. 4b). Increasing the d_m allows non–absorbed photons to be sent back into the structure in the active region and can advance the J_{ph} value. However, to make a more effective interpretation for J_{ph}, the AM 1.5G spectral irradiation should also be considered. An improvement in absorption occurs with the increase of d_m in the ST–OSC (Fig. 5a). Therefore, to better examine the effect of d_m on J_{ph}, a calculation should be made in the entire wavelength range of the AM 1.5G spectral irradiation for J_{ph}. The J_{ph} is calculated as follows:
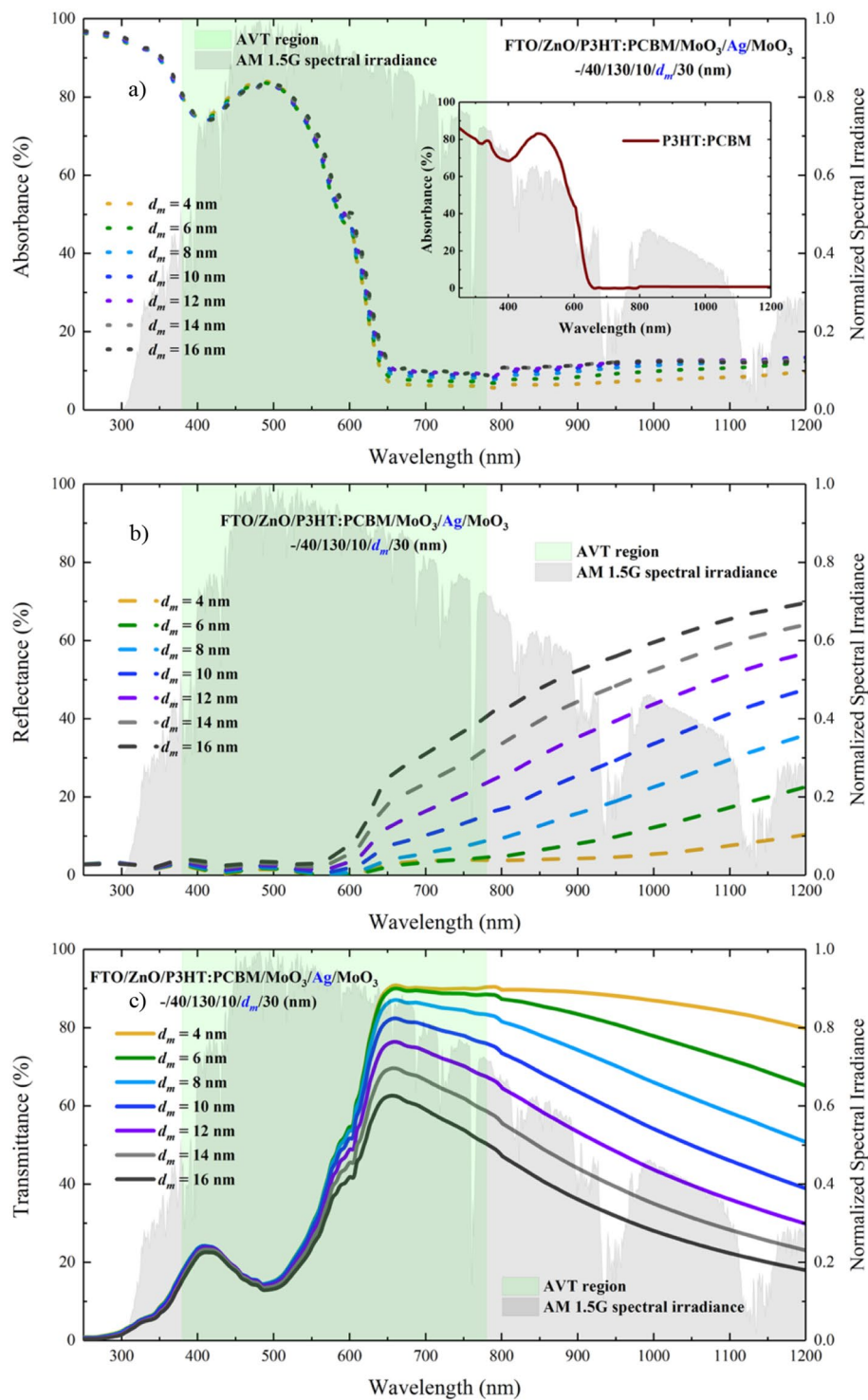
Figure 4. For FTO/ZnO/P3HT:PCBM/MoO$_3$/Ag/MoO$_3$ (–/40/130/10/d_m/30 nm) ST-OSC; (**a**) absorbance, (**b**) reflectance and (**c**) transmittance spectra. (**a**) Shows the absorbance spectrum of the P3HT:PCBM polymer blend that forms the active area of the inset ST-OSC.

$$J_{ph} = \int_{\lambda_{low}}^{\lambda_{up}} AM1.5G(\lambda)\ T(\lambda)\ \left(1 - e^{-\alpha(\lambda)d_{al}}\right)\ d\lambda \tag{1}$$

where $\alpha(\lambda)$ and d_{al} are the absorption coefficient and thickness of P3HT:PCBM, respectively. The J_{ph} change calculated based on d_m is given in Fig. 5b.
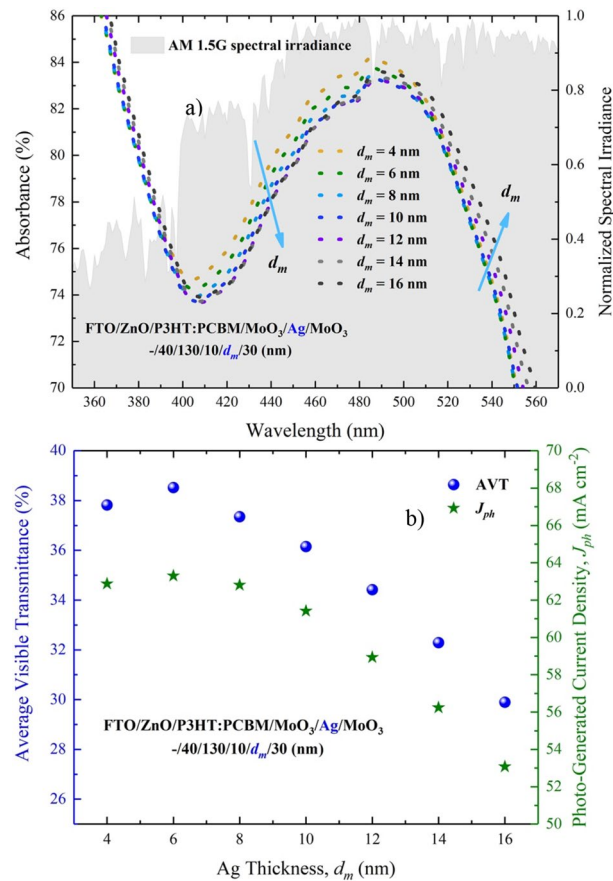
Figure 5. For FTO/ZnO/P3HT:PCBM/MoO$_3$/Ag/MoO$_3$ (–/40/130/10/d_m/30 nm) ST-OSC; (**a**) absorbance spectrum and, (**b**) changes of AVT and J_{ph} according to d_m.

We calculated the highest J_{ph} value for ST-OSC as 63.30 mA/cm^2 for d_m = 6 nm. The d_m adversely effects to J_{ph} in accordance decreasing absorption in the region where AM 1.5G spectral irradiance is high (Fig. 5a). We calculated AVT values, which are very important for ST-OSC, by using Eq. (16) (Fig. 5b). The highest AVT value of 38.52% was found for d_m = 6 nm. By reaching d_m = 16 nm, the AVT value decreasing 29.89% is even higher than 25%, which is the lower limit accepted for window applications. This result pointed out that the DMD designed at optimal values for P3HT:PCBM-based ST-OSCs is an appropriate contact.

The d_m behavior did not cause a serious change in the transmittance spectra for the wavelength region less than 500 nm. However, as seen in Fig. 4c, the increase in d_m caused a serious decrease in VR (longer than 500 nm) and NIR due to the reflective characteristics of Ag in the transmittance spectrum. AVT values are not directly influenced by these variations. The AVT value obtained for d_m = 4 nm is 37.82%, whereas the AVT value for d_m = 6 nm is 38.52% (Figs. 6 and 7). These values can be realized when the integral arguments in Fig. 6 and Eq. (16) are examined. No matter how much the transmittance varies during AM 1.5G, the values of the structures in the regions where the $V(\lambda) \times S_{AM1.5G}(\lambda)$ product intersects determine the changes in AVTs (Fig. 6). Within the orange hatched area representing the expression of $V(\lambda) \times S_{AM1.5G}(\lambda)$, the highest transmittance value belongs to the structure with d_m = 6 nm, and the AVT of this structure is at the highest value. The red arrow orientation in Fig. 6 indicates the variation of AVT.

When the ST-OSC is designed for d_m = 6 nm, it is noticeable as the most suitable structure in terms of both J_{ph} and AVT. However, the highest AVT value of the DMD was obtained for d_m = 8 nm. The AVT values obtained for both ST-OSC and DMD are comparatively given in Fig. 7. This inconsistency in the AVT, which occurs by simply investigating the DMD and integrating the DMD into the OSC, can be explained by the fact that the electromagnetic wave, which reaches the DMD structure, follows different paths due to reflection, refraction or absorption in different regions. In this case, it is an effective way to consider reaching the surface in which the angle and condition of the components of the electromagnetic wave that reflected, absorbed and eventually reached the DMD in the OSC.

Even with d_m reaching up 10 nm, there is a significant decrease of 22.3% in the AVT values. This result indicated that Ag has a remarkable effect on the optical characteristics of the ST-OSC.

We determined that the optimal value for Ag was d_m = 6 nm. Thus, to obtain a more detailed evaluation, we analyzed the effect of the d_{od}, on the AVT and J_{ph} values of the ST-OSC. The changes of the FTO/ZnO/P3HT:PCBM/MoO$_3$/Ag/MoO$_3$ (–/40/130/10/6/d_{od} nm) ST-OSC in d_{od}, AVT and J_{ph} are given in Fig. 8.
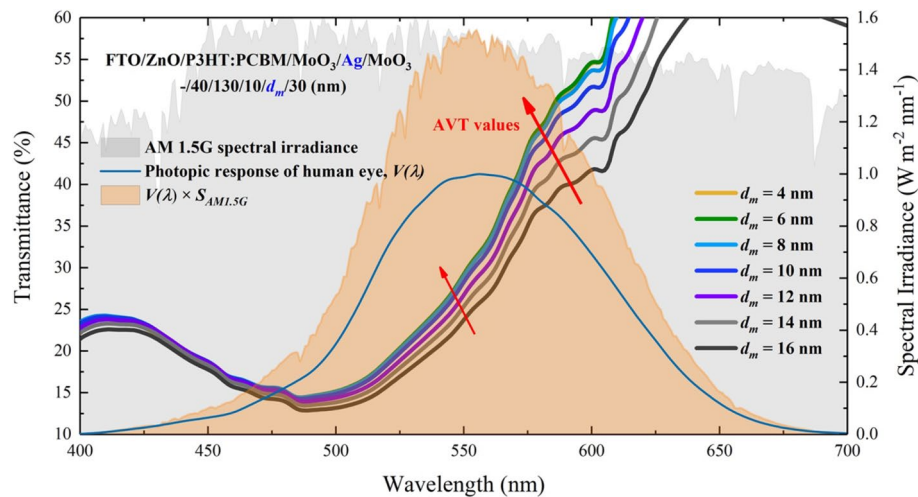
Figure 6. Transmittance spectra of FTO/ZnO/P3HT:PCBM/MoO$_3$/Ag/MoO$_3$. (–/40/130/10/d_m/30 nm) ST-OSC according to d_m and analysis of AVT values under $V(\lambda)$, AM 1.5G and $V(\lambda) \times S_{AM1.5G}(\lambda)$ changes. The orange shaded area is related to the change of $V(\lambda) \times S_{AM1.5G}(\lambda)$ and the area is the value of the integral in the denominator of Eq. (15).
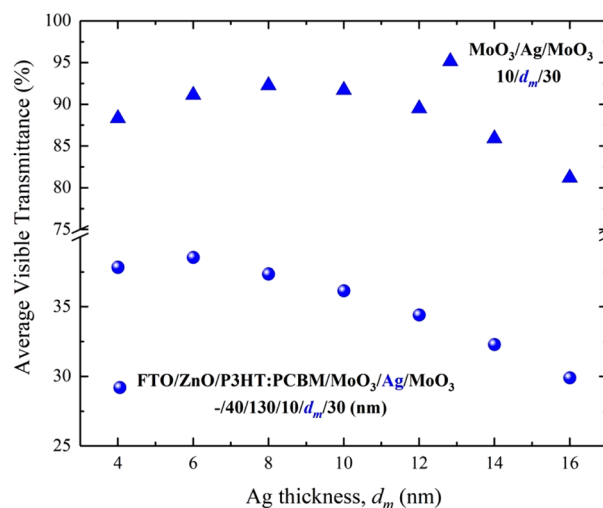

Figure 7. Comparative representation of the FTO/ZnO/P3HT:PCBM/MoO$_3$/Ag/MoO$_3$ (–/40/130/10/d_m /30 nm) ST-OSC and AVT values according to d_m of MoO$_3$/Ag/MoO$_3$ (10/d_m/30 nm).

As seen in Fig. 8, for the ST-OSC structure, although the change of d_{od} from 5 to 30 nm seems to cause a saturation in the AVT values, there is a slight decrease in the AVT values from 30 to 45 nm. The highest AVT value was obtained for $d_{od} = 30$ nm, and the value is 38.52%. Depending on d_{od}, this characteristic change in the AVT indicated that a high AVT value could be achieved for the ST-OSC structure designed for $d_{od} \geq 30$ nm. Although the J_{ph} value showed an improvement in d_{od} up to 20 nm, it was saturated after this value. We obtained the maximum J_{ph} of 63.30 mA/cm^2 for $d_{od} = 30$ nm. Even if AVT was still high in ST-OSCs designed for $d_{od} \geq$ 30 nm, there was a serious decrease in J_{ph}.

Considering the highest AVT and J_{ph} values for the ST-OSC, we obtained the structure with optimal values for $d_m = 6$ nm and $d_{od} = 30$ nm. Therefore, within the scope of the study, the investigated ST-OSC was produced at these values.

In addition, the d_{od} parameter does not affect the AVT of the ST-OSC as much as the Ag layer. Therefore, we examined the effect of Ag, which is the dominant layer in optical characteristics, on CIE 1931 chromaticity coordinates in ST-OSC.

When examining the colour coordinates, AM 1.5G's coordinates are $x = 0.32020$ and $y = 0.33240$, and D65's colour coordinates are $x = 0.3128$ and $y = 0.3290$. In the design of ST-OSCs with neutral colours for window applications, it is generally expected in order to get colour coordinates at the achromatic point ($x = 0.3333$ and $y = 0.3333$) or equal to the coordinates of AM 1.5G or D65[7]. In addition, the colour coordinates can be controlled
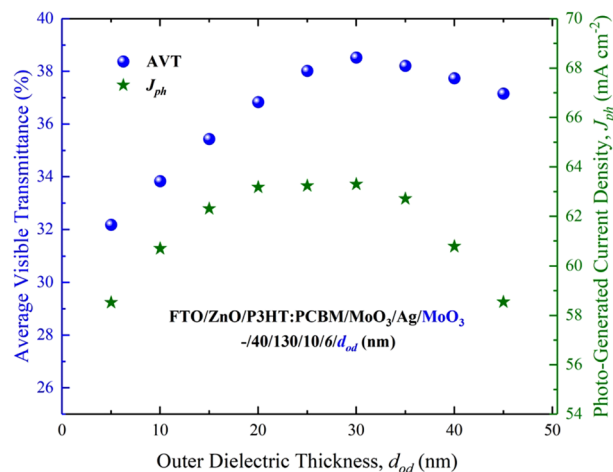
Figure 8. AVT and J_{ph} changes of FTO/ZnO/P3HT:PCBM/MoO$_3$/Ag/MoO$_3$. (–/40/130/10/6/d_{od} nm) ST-OSC according to d_{od}.

with transmittance spectra by the modification of the structure design. Thus, window applications with different colours can be obtained as a result of producing ST-OSCs in the desired colour.

According to the d_m changes of the ST-OSC, the locations and changes of the colour coordinates of the ST-OSC in the CIE 1931 chromaticity diagram under AM 1.5G illumination are given in Fig. 9a,b, respectively. It was clearly seen from the CIE chromaticity diagram that the change of d_m from 4 to 16 nm shifted the colour coordinates of the ST-OSC towards the D65 Planckian locus. The colour coordinates shifted from 0.468 to 0.445 for x and from 0.359 to 0.351 for y. We observed this change, which Ag makes in the colour coordinates of the ST-OSC, especially in x in Fig. 9c,d. As given in Fig. 9c, by increasing d_m, the transmittance of the ST-OSC in the region where it intersects with $\bar{x}(\lambda)$ decreased more than in the region where it intersects with $\bar{y}(\lambda)$. Therefore, the change in x would be greater. The effect of this change in transmittance was directly modified. Thus, the $T(\lambda) \, \bar{x}(\lambda)$ and $T(\lambda) \, \bar{y}(\lambda)$ factors appear in the integrants in Eqs. (17) and (18). The variation of the areas under the $T(\lambda) \, \bar{x}(\lambda)$ and $T(\lambda) \, \bar{y}(\lambda)$ factors with d_m directly presented the changes of x and y colour coordinates, respectively (Fig. 9d).

The CIE 1931 colour coordinates of ST-OSC for $d_m = 6$ nm and $d_{od} = 30$ nm with the highest AVT and J_{ph} were 0.4661 and 0.3587 for the x and y values, respectively. The schematic representation and photographs of the DMD, ST-OSC and opaque-OSC are given in Fig. 10a–c, respectively.

As seen in Fig. 10a, the top contact is quite transparent, and its colour selectivity is high. The photograph of the ST-OSC given in Fig. 10b indicates that the transmittance was high for all VR, and the colour selectivity was low in the red region of VR. This selectivity is not surprising according to the transmittance calculations made with TMM for this structure. The high transmittance in the calculated and experimental transmittance spectrum of the ST-OSC given in Fig. 11, especially for wavelengths higher than 550 nm, led us to determine the colour of the ST-OSC as red. On the other hand, it was seen from the photograph of the opaque-OSC produced with $d_m = 100$ nm in Fig. 10c that the structure was completely reflective but not transmittant. Especially for VR, electromagnetic waves entering by the glass are reflected back into the structure by the Ag layer, and the structure has opaque characteristics.

The calculated and experimental values of AVT obtained from the transmittance spectrum for the ST-OSC (Fig. 11). In addition, the x and y values obtained from the calculated transmittance spectrum and experimental transmittance spectrum for the CIE 1931 colour coordinates are given in Table 1.

J–V measurements of the opaque-OSC produced with $d_m = 100$ nm and of the ST-OSC produced for $d_m = 6$ nm and $d_{od} = 30$ nm are given in Fig. 12a,b, respectively. The cell output parameters of both structures are given in Table 2. FF values for both structures are above 50%. The thickness of the MoO$_3$ ($d_{id} = 10$ nm) layer serving as HTL in opaque and ST structures was the same, and there was no significant change in the V_{oc}, J_m and V_m values. However, the J_{sc} value was higher in the opaque structure compared to the ST structure. This can be explained by the re-absorption as a result of the reflection of photons, which entered the glass in the opaque-OSC and were not absorbed in the active layer, back into the structure from the opaque Ag. Thanks to the DMD in the ST-OSC, low reflectivity and high transmittance do not support the re-absorption process and a decrease in J_{sc} occurred.

Although a slightly lower efficiency of ST-OSCs compared to opaque-OSCs is a disadvantage for a device that converts electromagnetic energy into electrical energy, reduction in the efficiency is typically negligible for window applications with ST structure or when it is considered that OSC is obtained in different colours. Determining the optimal values for ST-OSC that works with the principle of photon absorption and allows the propagation of photons in the region that it absorbs is very important for electronic and optoelectronic applications.

Discussion

The main motivation of the study is to design and to produce a ST-OSC device. In designation process,we have presented that the MoO$_3$/Ag/MoO$_3$ DMD structure is a suitable top transparent contact for P3HT:PCBM-based OSCs by determining the optimal values of d_m and d_{od}. The fact that the transmittance values obtained for d_m
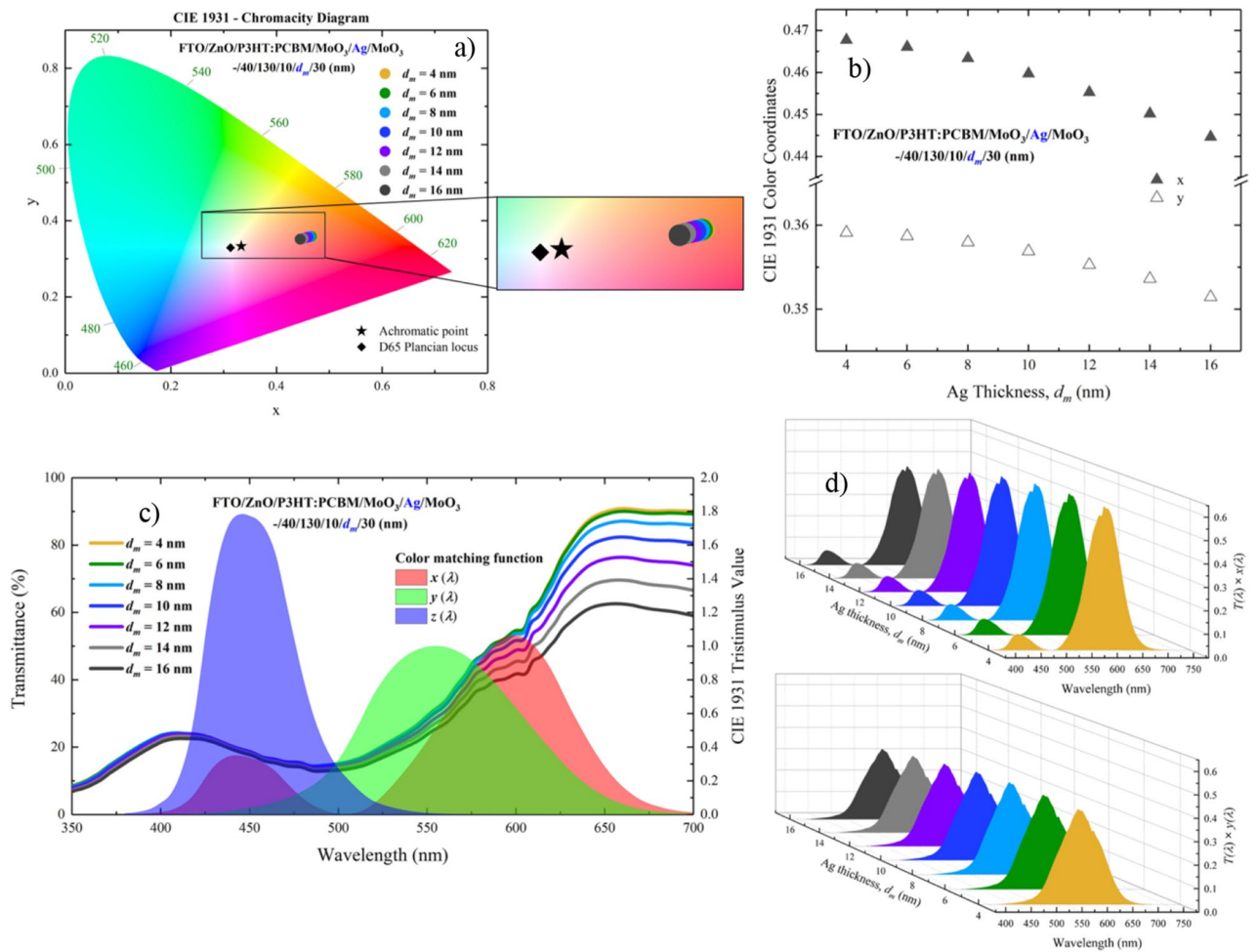
Figure 9. Calculations for FTO/ZnO/P3HT:PCBM/MoO$_3$/Ag/MoO$_3$ (−/40/130/10/d_m/10 nm) ST-OSC with different d_m; (**a**) the location of the color coordinates in the CIE 1931 chromaticity diagram, (**b**) the change of color coordinates, (**c**) the intersection of the transmittance characteristic of the ST-OSC with the $\bar{x}(\lambda)$, $\bar{y}(\lambda)$, $\bar{z}(\lambda)$ color matching functions, and (**d**) the change of $T(\lambda)\,\bar{x}(\lambda)$ ve $T(\lambda)\,\bar{y}(\lambda)$ functions.

in the range of 4–16 nm are quite high supports that the transmittance spectrum of DMD has the same trend as AM 1.5G spectral irradiance. Increasing the d_m value is enhanced the absorption and reflection of the ST-OSC in VR (wavelength above 560 nm) and NIR, indicating a trend of decrease in the transmittance spectrum. Furthermore, it can be concluded that the maximum transmittance of the ST-OSC structure is also reduced, since a significant decrease in the $\lambda_{\max}^{T}$ value of the DMD transmittance spectrum from 780 to 496 nm is observed.

The structure with $d_m = 6$ nm (with highest value of J_{ph}) and $d_{od} = 30$ nm is an optimal structure to be used in ST-OSCs by considering the AVT value is taken as a reference for window applications. We reported that the increment of d_m shifted the colour coordinates of the ST-OSC towards the D65 Planckian locus.

We have observed that no considerable change in the cell output parameters such as V_{oc}, J_{sc} as well as FF for both the opaque and ST-OSC structures produced. It is possible that the computed results of the parameters can said to be in good agreement with the results in the literature containing OSCs with an active layer of P3HT:PCBM[20,45].

Considering that the ST structure has a valuably utilization in window applications or OSCs obtained in different colours, the modification of opaque-OSC as the ST structure obviously make the decrease in PCE value negligible. Moreover, it is emphasized that we have obtained an effectively working ST-OSC in optoelectronic device applications.

Material and methods

Calculation of optical characteristics.
We performed the calculations by using the TMM, which is a highly effective method used in the simulations of optoelectronic devices. TMM is one of the important methods that analyze how the electromagnetic wave propagates within the structure and theoretically determine the optical characteristics of the structure, especially the DMD[49–51]. The position of the electric and magnetic field components within the DMD or OSC can be determined by a transfer matrix and propagation matrix[49]. While the electric and magnetic field components of the electromagnetic wave are connected to each other with a
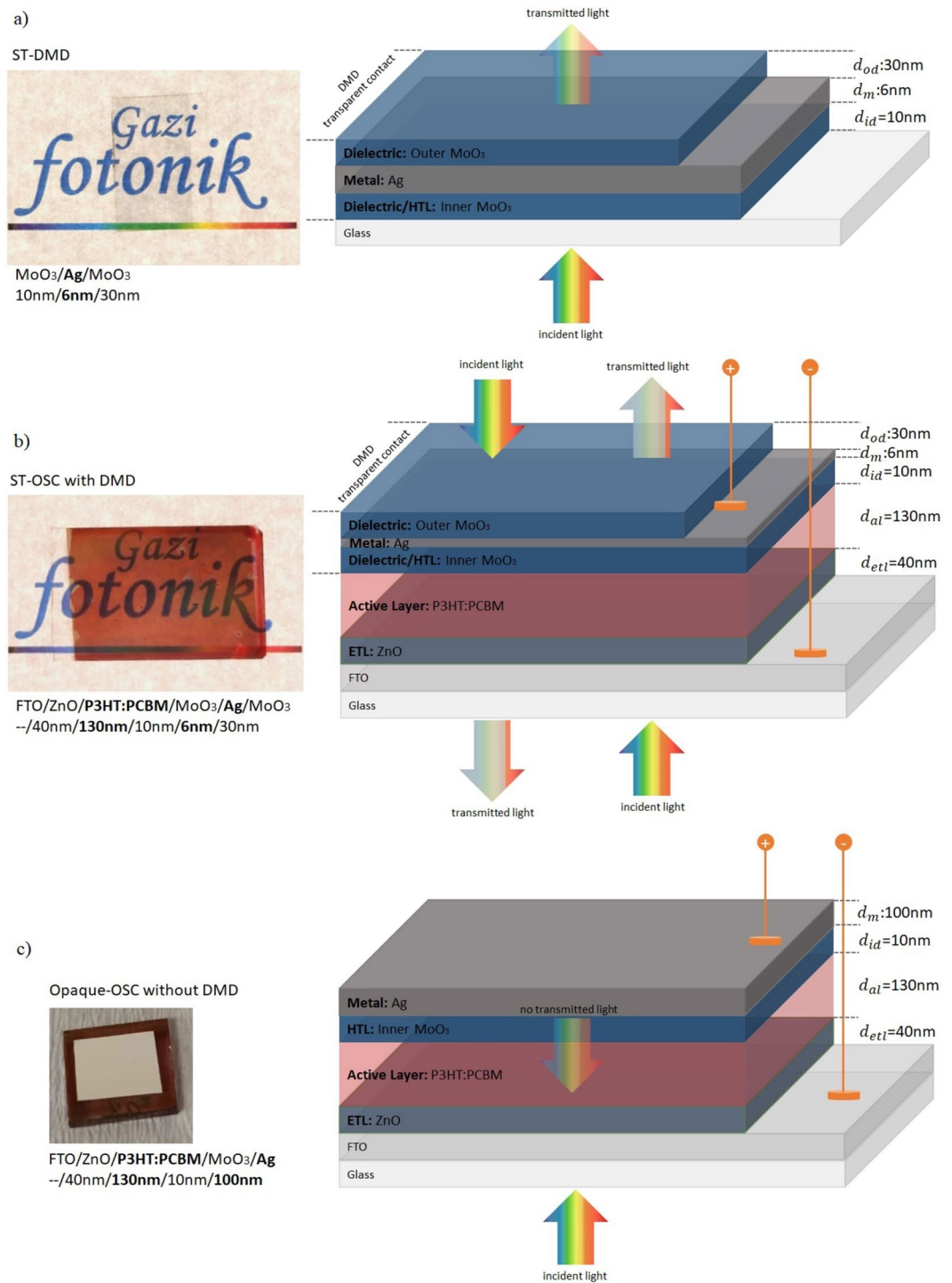
Figure 10. The photo and structure of; (**a**) the MoO₃/Ag/MoO₃ (10/6/30 nm) transparent top contact, (**b**) FTO/ZnO/P3HT:PCBM/MoO₃/Ag/MoO₃ (–/40/130/10/6/30 nm) ST-OSC, (**c**) FTO/ZnO/P3HT:PCBM/MoO₃/Ag (–/40/130/10/100 nm) opaque-OSC.

transfer matrix at each interface of the DMD layers, the spreading field components in the DMD are connected to each other by the propagation matrix.

As seen in Fig. 13, the metal layer surrounded by two dielectrics for the DMD structure has a conductivity (σ) distributed parallel to the $z = 0$ planes. It is necessary to examine the propagation of the electromagnetic wave on the interfaces of the conductor with the dielectrics. Assuming that the electromagnetic wave is polarized in the y direction and propagates in the z direction, the s and p polarizations can be examined. The magnetic field for polarization p can be written in the following form:
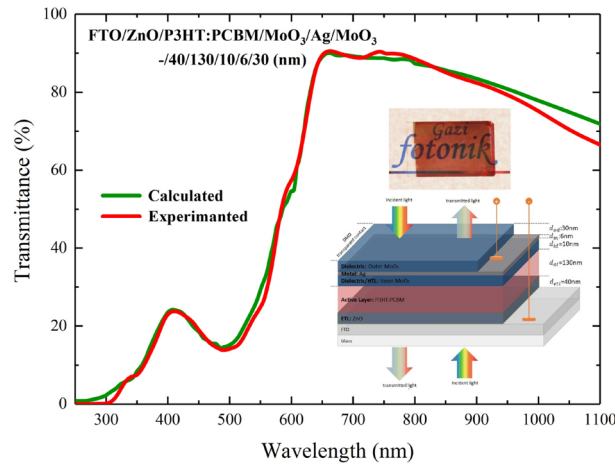
Figure 11. Calculated and experimental transmittance spectra of FTO/ZnO/P3HT:PCBM/MoO$_3$/Ag/MoO$_3$ (–/40/130/10/6/30 nm) ST-OSC.

	AVT (%)	CIE 1931 color coordinates	
		x	y
Calculated	38.52	0.4661	0.3587
Experimental	37.42	0.4613	0.3500

Table 1. AVT values and CIE 1931 color coordinates of FTO/ZnO/P3HT:PCBM/MoO$_3$/Ag/MoO$_3$ (–/40/130/10/6/30 nm) ST-OSC.

$$H_{1y} = \alpha_1 e^{i\vec{k}_1.\vec{r}} + \beta_1 e^{i\vec{k}_1.\vec{r}} = \left(\alpha_1 e^{ik_{1z}z} + \beta_1 e^{-ik_{1z}z}\right)e^{-ik_{1x}x}, \quad z < 0 \tag{2}$$

$$H_{2y} = \alpha_2 e^{i\vec{k}_2.\vec{r}} + \beta_2 e^{i\vec{k}_2.\vec{r}} = \left(\alpha_2 e^{ik_{2z}z} + \beta_2 e^{-ik_{2z}z}\right)e^{-ik_{2x}x}, \quad z > 0 \tag{3}$$

where $\vec{k}_i = \sqrt{\varepsilon_i}\omega/c$ $(i = 1, \ 2)$ is the wave vector of the electromagnetic wave, ε_i $(i = 1, \ 2)$ is the dielectric constant of the medium, ω is the angular frequency, c is the propagation velocity of the electromagnetic wave in space and α_i and β_i $(i = 1, \ 2)$ are the coefficients. According to Snell's law, the x components of the wave vector in both media at the interface will be equal to each other: $k_{1x} = k_{2x}$. If we also apply the boundary conditions of the electric field and the magnetic field for the interface[52], we obtain the equations found below:

$$\hat{n}_s \times (\vec{E}_2 - \vec{E}_1)\big|_{z=0} = 0 \tag{4}$$

$$\hat{n}_s \times (\vec{H}_2 - \vec{H}_1)\big|_{z=0} = \vec{J} \tag{5}$$

Here, $\hat{n}_s$ is the normal unit vector of the surface, and $\vec{J}$ is the surface current density of the metallic layer. In addition, by obtaining $\vec{J}$ by Ohm's law and applying the $z = 0$ condition, the following equations are obtained:

$$\frac{k_{1z}}{\varepsilon_1}(a_1 - b_1) - \frac{k_{2z}}{\varepsilon_2}(a_2 - b_2) = 0 \tag{6}$$

$$(a_1 + b_1) - (a_2 + b_2) = J_x \tag{7}$$

$$J_x = \sigma E_x\big|_{z=0} = \frac{\sigma k_{2z}}{\varepsilon_0 \varepsilon_2 \omega}(a_2 - b_2) \tag{8}$$

where ε_0 is the permittivity of the space. By combination of Eqs. (6), (7) and (8), a_i and b_i $(i = 1)$ can be associated with a_{i+1}, b_{i+1} and the transition matrix $M_{i\rightarrow i+1}$.
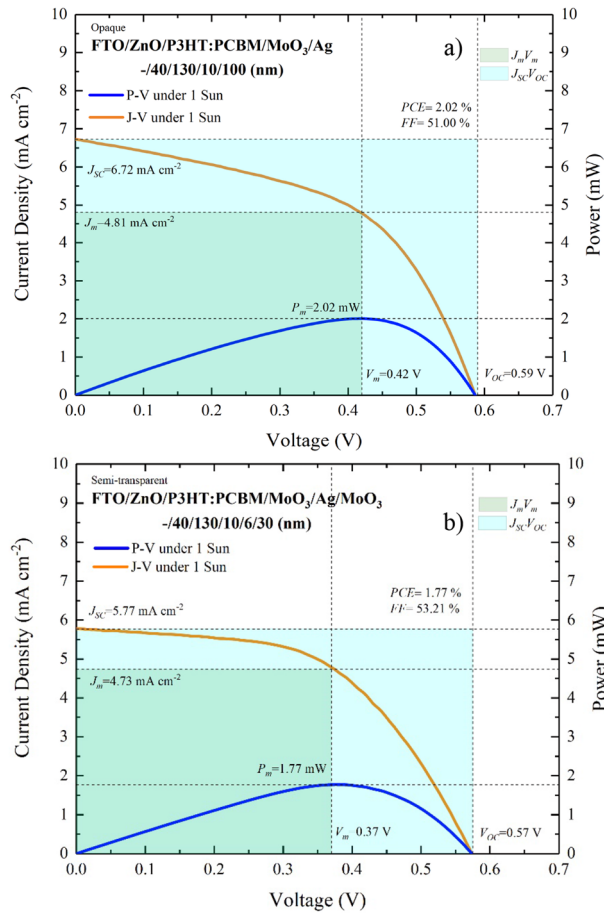
Figure 12. $J - V$ characteristics of (**a**) FTO/ZnO/P3HT:PCBM/MoO$_3$/Ag (–/40/130/10/100 nm) opaque-OSC and (**b**) FTO/ZnO/P3HT:PCBM/MoO$_3$/Ag/MoO$_3$ (–/40/130/10/6/30 nm) ST-OSC.

	J_{sc} (mA cm^{-2})	J_m (mA cm^{-2})	V_{oc} (V)	V_m (V)	P_m (mW)	FF (%)	PCE (%)
ST-OSC	5.77	4.73	0.57	0.37	1.77	53.21	1.77
Opaque-OSC	6.72	4.81	0.59	0.42	2.02	51.00	2.02

Table 2. The cell output parameters of (a) FTO/ZnO/P3HT:PCBM/MoO$_3$/Ag (–/40/130/10/100 nm) opaque-OSC and, (b) FTO/ZnO/P3HT:PCBM/MoO$_3$/Ag/MoO$_3$ (–/40/130/10/6/30 nm) ST-OSC.

$$\begin{pmatrix} a_i \\ b_i \end{pmatrix} = M_{i \to i+1} \begin{pmatrix} a_{i+1} \\ b_{i+1} \end{pmatrix} \tag{9}$$

The $M_{i \to i+1}$ transition matrix is $M_{1 \to 2}$ as follows when $i = 1$ is selected for DMD design with a single metallic layer:

$$M_{1 \to 2} = \frac{1}{2} \begin{pmatrix} 1 + n_p + \xi_p & 1 - n_p - \xi_p \\ 1 - n_p + \xi_p & 1 + n_p - \xi_p \end{pmatrix} \tag{10}$$

where $n_p = \frac{\varepsilon_1 k_{2z}}{\varepsilon_2 k_{1z}}$, and $\xi_p = \frac{\sigma k_{2z}}{\varepsilon_0 \varepsilon_2 \omega}$. The above magnetic field and related boundary conditions for polarization p and all processes performed by the application of Ohm's law are also applicable to the electric field component for s polarization. In this case, again by using Ohm's law and boundary conditions, the transition matrix of s polarization is obtained as follows:

$$M_{1 \to 2} = \frac{1}{2} \begin{pmatrix} 1 + n_s + \xi_s & 1 - n_s + \xi_s \\ 1 - n_s - \xi_s & 1 + n_s - \xi_s \end{pmatrix} \tag{11}$$

where μ_0 is the transmittance of the space, the parameters n_s and ξ_s are equal to the terms $\frac{k_{2z}}{k_{1z}}$ and $\frac{\sigma \mu_0 \omega}{k_{1z}}$, respectively. The n_p and n_s terms used in the derivation of the equations are directly related to the refractive index of the
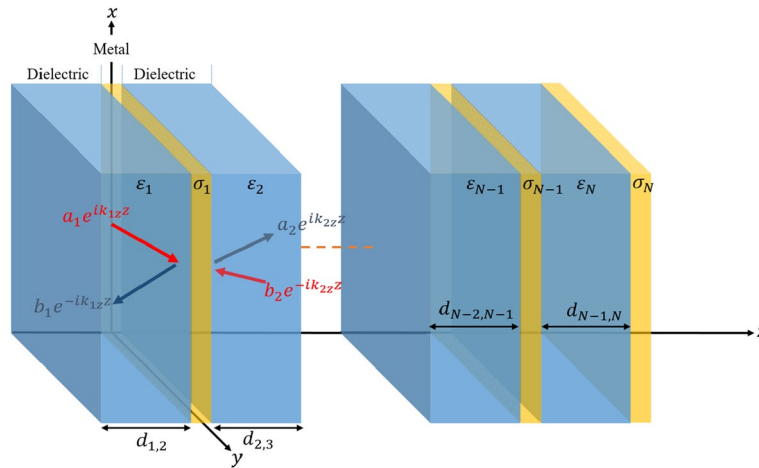
Figure 13. A thin metal layer with σ conductivity surrounded by two dielectric layers with values ε_1 and ε_2. The structure is self-repeatable and can be reduced to a DMD structure for a single metal layer. Red and blue arrows represent the electromagnetic wave at the interface and at the reflected, respectively.

layers and include the absorption coefficient within the complex term. These values depend on the wavelength and the angle of incidence of the electromagnetic wave.

Considering the equations, the transition matrices obtained for both s and p polarizations are the same, except for the sign difference in non-diagonal components. By making the necessary arrangements for $j = (s, \ p)$ and $\eta_p = 1, \eta_s = -1$, a common transition matrix can be parameterized as follows:

$$M_{1\to 2} = \frac{1}{2}\begin{pmatrix} 1 + n_j + \xi_j & 1 - n_j - \eta_j\xi_j \\ 1 - n_j + \eta_j\xi_j & 1 + n_j - \xi_j \end{pmatrix} \tag{12}$$

The relationship between the transition (t) and reflection (r) coefficients of the electromagnetic wave at the interfaces with the transition matrix as well as the transmittance (T) and reflection (R) spectrum of the DMD and ST-OSC structures can be calculated as follows:

$$R = |r|^2 = \left| \frac{M_{2\to 1}}{M_{1\to 1}} \right|^2 \tag{13}$$

$$T = |t|^2 = \left| \frac{1}{M_{1\to 1}} \right|^2 \tag{14}$$

In addition, obtaining the T and R spectrum of the structures enables the absorption (A) spectrum to be obtained by the following:

$$A = 1 - (T + R) \tag{15}$$

Determination of average visible transmittance. The transparency properties of ST-OSCs are determined by both AVT values and by transmittance characteristics in the visible light wavelength range (370–740 nm), taking into account the photonic response of the human eye ($V(\lambda)$). The AVT value is calculated by the following formula[7,53]:

$$AVT = \frac{\int_{370 \ nm}^{780 \ nm} T(\lambda) \, V(\lambda) \, S_{AM1.5G}(\lambda) \, d\lambda}{\int_{370 \ nm}^{780 \ nm} V(\lambda) \, S_{AM1.5G}(\lambda) \, d\lambda} \tag{16}$$

where $S_{AM1.5G}(\lambda)$ is the photon flux under AM 1.5G illumination (Fig. 3). AVT values depend on the working environment of ST-OSCs, and an AVT value of 25% is an acceptable criterion for window applications[7,21]. In addition, if an experimental result is to be obtained in AVT calculation, the T (λ) value to be used should be experimental, and the beam spot must be within the effective area during the measurement. If the spot area is larger than the effective area, some of the incident light may directly reach the detector and experimentally create an error in the transmittance measurement[7,54].

Evaluation of color coordinates of ST-OSC. Another characteristic of ST-OSCs as important as the AVT is the colour coordinates (x, y) in the CIE 1931 chromaticity diagram. The diagram is designed based on the response of the human eye and is often used to determine the colour characteristics of illuminators[7]. For ST-OSCs, the colour coordinates of the OSC were determined using the CIE 1931 chromaticity diagram under AM
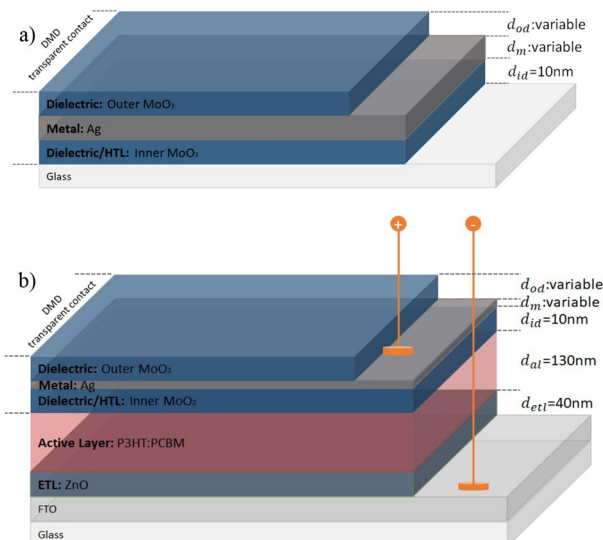
Figure 14. Schematic representation of (**a**) MoO$_3$/Ag/MoO$_3$ DMD transparent top contact and, (**b**) FTO/ZnO/P3HT:PCBM/MoO$_3$/Ag/MoO$_3$ ST-OSC.

1.5G illumination[55]. In the tristimulus system, X, Y and Z values can be calculated under VR with the following equations:

$$X = \int_{370\ nm}^{780\ nm} S_{AM1.5G}^{D65}(\lambda)\ T(\lambda)\ \bar{x}(\lambda)\ \ d\lambda \tag{17}$$

$$Y = \int_{370\ nm}^{780\ nm} S_{AM1.5G}^{D65}(\lambda)\ T(\lambda)\ \bar{y}(\lambda)\ d\lambda \tag{18}$$

$$Z = \int_{370\ nm}^{780\ nm} S_{AM1.5G}^{D65}(\lambda)\ T(\lambda)\ \bar{z}(\lambda)\ \ d\lambda \tag{19}$$

In all these equations, $S_{AM1.5G}^{D65}$ is the CIE standard D65 illuminant spectrum, and the terms $\bar{x}(\lambda)$, $\bar{y}(\lambda)$ and $\bar{z}(\lambda)$ are colour-matching functions defined by the CIE protocol $(X + Y + Z) = 1$ and the colour coordinates can be simplified to two-dimensional coordinates[56]:

$$x = \frac{X}{(X + Y + Z)} \tag{20}$$

$$y = \frac{Y}{(X + Y + Z)} \tag{21}$$

Experimental details. In the scope of study, ST-OSCs and opaque-OSCs have the active region, which is the blend of poly 3-hexylthiophene-2, 5-diyl (P3HT) and poly 6, 6-phenyl C61-butyric acid methyl ester (PCBM). Except for the structure and design of upper electrodes, all structure parameters are the same. The structure of OSC, active region and top transparent contacts are formed as inverted device, bulk-heterojunction and DMD, respectively (Fig. 14a,b). All layers in the OSC structures, except the active region, were coated using the Nanovak NVTS500 Sputtering system.

When used as the bottom electrode, fluorine tin oxide (FTO) coated on glass has a high optical transmittance (about 90%) and low work function (~ 4.4 eV) as well as being electrically conductive[57]. Before SC production, we cleaned glass substrates coated with FTO of organic and inorganic contaminants. In the cleaning process, we ultrasonically immersed the substrates in detergent and deionized water for 5 min, and then rinsed with distilled water. We then cleaned the samples with pure acetone and isopropyl alcohol for 10 min in different containers in an ultrasonic bath and again rinsed them with deionized water. In the last process, we dried FTO substrates with high-purity nitrogen (N$_2$) gas and made a metal oxide coating.

We used a ZnO layer as ETL due to its high optical transmittance in the VR and NIR regions and high carrier mobility (0.066 cm^2 V^{-1} s^{-1})[58–60]. We made the deposition of ZnO with the sputtering technique using a

ZnO target with a purity of 99.999%. To get high optical transmittance, the thickness (d_{etl}) of ETL was set to 40 nm. We coated the active region of SCs with the spin coating technique using P3HT:PCBM. We prepared the solution from the ready-made P3HT and PCBM polymers by blending them evenly by means of mass and adding dichlorobenzene solvent at a concentration of 20 mg/mL. We allowed this to mix homogeneously with a magnetic stirrer for 14 h at 80 °C. For all OSCs, we set P3HT:PCBM active layer thickness (d_{al}) as 130 nm. We used MoO_3 as HTL. For the produced opaque-OSC, the MoO_3 layer acts exactly as an HTL. However, this situation differs for ST-OSC in that MoO_3 forms both the HTL and the inner part in the DMD. The HTL layer prevents a possible penetration of the metal of the DMD for ST-OSC or the metal for opaque-OSC towards the active layer. It also functions as an electron-blocking layer in its structures. We determined the thickness of the HTL layer ($d_{htl} = d_{id}$) in all structures as 10 nm. We created the Ag for opaque-OSC using the 100 nm thick by sputtering technique. We produced $MoO_3/Ag/MoO_3$ for ST-OSC using the sputtering technique with $d_{id} = 10$ nm and optimal d_m and d_{od} thicknesses as determined by our calculations. The high purity (99.999%) of MoO_3 and Ag targets were used.

We determined the optical characteristics of the produced structures with a Perkin Elmer Lambda 2S UV–Vis–NIR spectrometer in the 300–1100 nm wavelength range. In addition, we used the Keithley 4200 source meter for current density–voltage (J–V) measurements and the Newport Oriel-Sol1A solar simulator for AM 1.5G illumination.

Data availability

The datasets generated during and/or analysed during the current study are available from the corresponding author (Ç.Ç.) on reasonable request.

References

1. Hau, S. K., Yip, H.-L. & Jen, A.K.-Y. A review on the development of the inverted polymer solar cell architecture. *Polym. Rev.* **50**, 474–510 (2010).
2. Yang, X. *et al.* High-efficiency polymer solar cells achieved by doping plasmonic metallic nanoparticles into dual charge selecting interfacial layers to enhance light trapping. *Adv. Energy Mater.* **3**, 666–673 (2013).
3. Alem, S. *et al.* Effect of mixed solvents on PCDTBT:PC70BM based solar cells. *Org. Electron.* **12**, 1788–1793 (2011).
4. Brabec, C. J., Sariciftci, N. S. & Hummelen, J. C. Plastic solar cells. *Adv. Funct. Mater.* **11**, 15–26 (2001).
5. Choi, H. *et al.* Acid-functionalized fullerenes used as interfacial layer materials in inverted polymer solar cells. *Org. Electron.* **14**, 3138–3145 (2013).
6. Liu, Q. *et al.* 18% Efficiency organic solar cells. *Sci. Bull.* **65**, 272–275 (2020).
7. Hu, Z. *et al.* A critical review on semitransparent organic solar cells. *Nano Energy* **78**, 105376 (2020).
8. Ma, X. *et al.* Highly efficient quaternary organic photovoltaics by optimizing photogenerated exciton distribution and active layer morphology. *Nano Energy* **70**, 104496 (2020).
9. Gao, W. *et al.* Thick-film organic solar cells achieving over 11% efficiency and nearly 70% fill factor at thickness over 400 nm. *Adv. Funct. Mater.* **30**, 1908336 (2020).
10. Cheng, P. *et al.* Alloy acceptor: Superior alternative to PCBM toward efficient and stable organic solar cells. *Adv. Mater.* **28**, 8021–8028 (2016).
11. Zhang, M. *et al.* Highly efficient ternary polymer solar cells by optimizing photon harvesting and charge carrier transport. *Nano Energy* **22**, 241–254 (2016).
12. Hu, Z. *et al.* Ternary nonfullerene polymer solar cells with a power conversion efficiency of 11.6% by inheriting the advantages of binary cells. *ACS Energy Lett.* **3**, 555–561 (2018).
13. An, Q. *et al.* High-efficiency and air stable fullerene-free ternary organic solar cells. *Nano Energy* **45**, 177–183 (2018).
14. Chang, L. *et al.* Optimising non-patterned $MoO_3/Ag/MoO_3$ anode for high-performance semi-transparent organic solar cells towards window applications. *Nanomaterials* **10**, 1759 (2020).
15. Tian, X. *et al.* Semitransparent inverted organic solar cell with improved absorption and reasonable transparency perception based on the nanopatterned $MoO_3/Ag/MoO_3$ anode. *J. Nanophotonics* **9**, 093043 (2015).
16. Xiong, Y. *et al.* Semi-transparent organic solar cells for greenhouse application (Conference Presentation). in *Organic, Hybrid, and Perovskite Photovoltaics XX* vol. 11094 110940N (International Society for Optics and Photonics, 2019).
17. Joseph, B., Pogrebnaya, T. & Kichonge, B. Semitransparent building-integrated photovoltaic: Review on energy performance, challenges, and future potential. *Int. J. Photoenergy* **2019**, 1–17 (2019).
18. Upama, M. B. *et al.* High performance semitransparent organic solar cells with 5% PCE using non-patterned $MoO_3/Ag/MoO_3$ anode. *Curr. Appl. Phys.* **17**, 298–305 (2017).
19. Jeon, I. *et al.* Metal-electrode-free window-like organic solar cells with p-doped carbon nanotube thin-film electrodes. *Sci. Rep.* **6**, 31348 (2016).
20. Cho, J. M., Lee, S. K., Moon, S.-J., Jo, J. & Shin, W. S. $MoO_3/Ag/MoO_3$ top anode structure for semitransparent inverted organic solar cells. *Curr. Appl. Phys.* **14**, 1144–1148 (2014).
21. Chen, K.-S. *et al.* Semi-transparent polymer solar cells with 6% PCE, 25% average visible transmittance and a color rendering index close to 100 for power generating window applications. *Energy Environ. Sci.* **5**, 9551 (2012).
22. Drolet, N. Organic photovoltaic: Efficiency and lifetime challenges for commercial viability. in *2012 MRS Spring Meeting and Exhibit, San Francisco, CA, Moscone West Convention Center, Marriott Marquis* (2012).
23. Ji, C., Liu, D., Zhang, C. & Jay Guo, L. Ultrathin-metal-film-based transparent electrodes with relative transmittance surpassing 100%. *Nat. Commun.* **11**, 3367 (2020).
24. Zhang, C. *et al.* An ultrathin, smooth, and low-loss Al-doped Ag film and its application as a transparent electrode in organic photovoltaics. *Adv. Mater.* **26**, 5696–5701 (2014).
25. Zhao, D., Zhang, C., Kim, H. & Guo, L. J. High-performance Ta_2O_5/Al-doped Ag electrode for resonant light harvesting in efficient organic solar cells. *Adv. Energy Mater.* **5**, 1500768 (2015).
26. Bauch, M. & Dimopoulos, T. Design of ultrathin metal-based transparent electrodes including the impact of interface roughness. *Mater. Des.* **104**, 37–42 (2016).
27. Kinner, L. *et al.* Polymer interlayers on flexible PET substrates enabling ultra-high performance, ITO-free dielectric/metal/dielectric transparent electrode. *Mater. Des.* **168**, 107663 (2019).
28. Guillén, C. & Herrero, J. TCO/metal/TCO structures for energy and flexible electronics. *Thin Solid Films* **520**, 1–17 (2011).

29. Maniyara, R. A., Mkhitaryan, V. K., Chen, T. L., Ghosh, D. S. & Pruneri, V. An antireflection transparent conductor with ultralow optical loss (<2 %) and electrical resistance (<6 Ω sq⁻¹). *Nat. Commun.* **7**, 13771 (2016).
30. Dalapati, G. K. *et al.* Transparent heat regulating (THR) materials and coatings for energy saving window applications: Impact of materials design, micro-structural, and interface quality on the THR performance. *Prog. Mater. Sci.* **95**, 42–131 (2018).
31. Zhang, C. *et al.* High-performance doped silver films: Overcoming fundamental material limits for nanophotonic applications. *Adv. Mater.* **29**, 1605177 (2017).
32. Wang, Z. *et al.* Metal-enhanced adsorption of high-density polyelectrolyte nucleation-inducing seed layer for highly conductive transparent ultrathin metal films. *Front. Mater.* **6**, 1–9 (2019).
33. Cao, W., Li, J., Chen, H. & Xue, J. Transparent electrodes for organic optoelectronic devices: A review. *J. Photonics Energy* **4**, 040990 (2014).
34. Zilberberg, K. & Riedl, T. Metal-nanostructures—A modern and powerful platform to create transparent electrodes for thin-film photovoltaics. *J. Mater. Chem. A* **4**, 14481–14508 (2016).
35. Kim, S. & Lee, J.-L. Design of dielectric/metal/dielectric transparent electrodes for flexible electronics. *J. Photonics Energy* **2**, 21215 (2012).
36. Ham, J., Kim, S., Jung, G. H., Dong, W. J. & Lee, J.-L. Design of broadband transparent electrodes for flexible organic solar cells. *J. Mater. Chem. A* **1**, 3076 (2013).
37. Upama, M. B. *et al.* High-efficiency semitransparent organic solar cells with non-fullerene acceptor for window application. *ACS Photonics* **4**, 2327–2334 (2017).
38. Tao, C. *et al.* Semitransparent inverted polymer solar cells with MoO₃/Ag/MoO₃ as transparent electrode. *Appl. Phys. Lett.* **95**, 053303 (2009).
39. Upama, M. B. *et al.* Low-temperature processed efficient and colourful semitransparent perovskite solar cells for building integration and tandem applications. *Org. Electron.* **65**, 401–411 (2019).
40. Cattin, L., Louarn, G., Morsli, M. & Bernède, J. C. Semi-transparent organic photovoltaic cells with dielectric/metal/dielectric top electrode: Influence of the metal on their performances. *Nanomaterials* **11**, 393 (2021).
41. Guillén, C. & Herrero, J. ITO/metal/ITO multilayer structures based on Ag and Cu metal films for high-performance transparent electrodes. *Sol. Energy Mater. Sol. Cells* **92**, 938–941 (2008).
42. Betancur, R. *et al.* Transparent polymer solar cells employing a layered light-trapping architecture. *Nat. Photonics* **7**, 995–1000 (2013).
43. Yu, W. *et al.* Highly efficient semitransparent polymer solar cells with color rendering index approaching 100 using one-dimensional photonic crystal. *ACS Appl. Mater. Interfaces* **7**, 9920–9928 (2015).
44. Nguyen, D.-T. *et al.* Effect of the thickness of the MoO₃ layers on optical properties of MoO₃/Ag/MoO₃ multilayer structures. *J. Appl. Phys.* **112**, 063505 (2012).
45. Li, F. *et al.* Semitransparent inverted polymer solar cells employing a sol-gel-derived TiO2 electron-selective layer on FTO and MoO₃/Ag/MoO₃ transparent electrode. *Nanoscale Res. Lett.* **9**, 579 (2014).
46. Wang, Z. *et al.* Improvement of transparent silver thin film anodes for organic solar cells with a decreased percolation threshold of silver. *Sol. Energy Mater. Sol. Cells* **127**, 193–200 (2014).
47. Wang, Z. *et al.* Flexible ITO-free organic solar cells based on MoO₃/Ag anodes. *IEEE Photonics J.* **7**, 1–9 (2015).
48. Kim, H., Lee, K.-T., Zhao, C., Guo, L. J. & Kanicki, J. Top illuminated organic photodetectors with dielectric/metal/dielectric transparent anode. *Org. Electron.* **20**, 103–111 (2015).
49. Zhan, T., Shi, X., Dai, Y., Liu, X. & Zi, J. Transfer matrix method for optics in graphene layers. *J. Phys. Condens. Matter* **25**, 215301 (2013).
50. Yan, H. *et al.* Tunable infrared plasmonic devices using graphene/insulator stacks. *Nat. Nanotechnol.* **7**, 330–334 (2012).
51. Bonaccorso, F., Sun, Z., Hasan, T. & Ferrari, A. C. Graphene photonics and optoelectronics. *Nat. Photonics* **4**, 611–622 (2010).
52. Yeh, P. *Optical Waves in Layered Media* Vol. 95 (Wiley, 1988).
53. Brus, V. V. *et al.* Solution-processed semitransparent organic photovoltaics: From molecular design to device performance. *Adv. Mater.* **31**, 1900904 (2019).
54. Yang, C., Liu, D., Bates, M., Barr, M. C. & Lunt, R. R. How to accurately report transparent solar cells. *Joule* **3**, 1803–1809 (2019).
55. Ameri, T. *et al.* Fabrication, optical modeling, and color characterization of semitransparent bulk-heterojunction organic solar cells in an inverted structure. *Adv. Funct. Mater.* **20**, 1592–1598 (2010).
56. Shin, D. & Choi, S.-H. Recent studies of semitransparent solar cells. *Coatings* **8**, 329 (2018).
57. Andersson, A. *et al.* Fluorine tin oxide as an alternative to indium tin oxide in polymer LEDs. *Adv. Mater.* **10**, 859–863 (1998).
58. Machrafi, H. *Organic Solar Cells* (Springer, 2013).
59. White, M. S., Olson, D. C., Shaheen, S. E., Kopidakis, N. & Ginley, D. S. Inverted bulk-heterojunction organic photovoltaic device using a solution-derived ZnO underlayer. *Appl. Phys. Lett.* **89**, 143517 (2006).
60. Roest, A. L., Kelly, J. J., Vanmaekelbergh, D. & Meulenkamp, E. A. Staircase in the electron mobility of a ZnO quantum dot assembly due to shell filling. *Phys. Rev. Lett.* **89**, 036801 (2002).

Acknowledgements

Author contributions

Ç.Ç. conceived the idea, conducted the study, performed the calculations and designed the ST-OSCs, fabricated the solar cell structures, wrote the main manuscript text, E.Ç. performed the calculations, designed the ST-OSCs, B.K. performed and analyzed the UV–Visible experiment and wrote the main manuscript text, F.G. interpreted the optical spectra and did the critical revision of the manuscript, Y.Ö. fabricated the solar cell structures, performed *J–V* experiments, H.İ.E. fabricated the solar cell structures. İ.C. fabricated the solar cell structures, S.E. evaluated the calculation of color coordinates, S.Ö. supervised the study. All authors reviewed the manuscript.

Competing interests

The authors declare no competing interests.

Additional information

Correspondence and requests for materials should be addressed to Ç.Ç.

Reprints and permissions information is available at www.nature.com/reprints.

Publisher's note Springer Nature remains neutral with regard to jurisdictional claims in published maps and institutional affiliations.